PERGAMON

International Journal of Heat and Mass Transfer 44 (2001) 3843–3853

International Journal of HEAT and MASS TRANSFER

www.elsevier.com/locate/ijhmt

Interferometric probing of rapid vaporization at a solid–liquid interface induced by pulsed-laser irradiation

Dongsik Kim *, Hee K. Park [1], Costas P. Grigoropoulos

Department of Mechanical Engineering, University of California, Berkeley, CA 94720, USA

Received 7 July 2000; received in revised form 2 January 2001

Abstract

In situ monitoring of rapid vaporization process on a submicron length scale is essential for understanding the phenomena induced by pulsed-laser heating of solid surfaces in contact with liquids. A number of laser-processing applications including steam laser cleaning and liquid-assisted material ablation take advantage of enhanced acoustic excitation in the explosive vaporization process. In this paper, a novel technique based on Michelson interferometry is developed to study the liquid vaporization process induced by a KrF excimer-laser pulse ($\lambda = 248$ nm, full-width-half-maximum (FWHM) = 24 ns) at relatively low fluences typically used for laser cleaning processes. The dynamics of rapid vaporization in a highly superheated liquid layer is measured in a semi-quantitative manner. In addition, optical-reflectance and forward-scattering measurements are performed to elucidate the vaporization dynamics. The results suggest that separate bubble nuclei begin to grow in the early stage of vaporization and tend to coalesce later. The maximum bubble size and growth rate are estimated to be of the order of 0.1 μm and 1 m/s, respectively. The bubbles decay at a significantly slow rate in comparison with the growth rate. The interference probe detects the long-term acoustic cavitation, so called memory effect, more effectively than the previously employed reflectance probe. This study reveals that the acoustic enhancement in the laser induced vaporization process is caused by bubble expansion in the initial growth stage, not by bubble collapse. © 2001 Published by Elsevier Science Ltd.

1. Introduction

The kinetics of rapid vaporization of liquid subjected to a high-heat flux has long been a subject of intense research interest [1–3]. Recently, rapid vaporization of liquid at a solid/liquid interface has become an important issue in pulsed-laser thermal processing assisted by a liquid film. The rapid liquid vaporization constitutes a critical step in the laser cleaning and ablation processes assisted by a liquid layer [4–8]. Laser pulse irradiation on a solid surface in contact with liquid, and subsequent liquid vaporization, results in photoacoustic excitation, generating an augmented pressure pulse. The pressure pulse produced in the explosive liquid vaporization is utilized in the liquid-assisted processes at relatively low laser fluences. Consequently, in situ detection of rapid vaporization on a submicron length scale is essential for understanding the physical mechanisms of laser–surface interaction. In this study, a novel optical probe is developed to monitor the dynamics of rapid vaporization process induced by a laser pulse (temperature increase of the order of 10^9°C/s). Based on the experimental results, the vaporization process on a solid surface is analyzed. Experiments are performed at relatively low laser fluences, with emphasis on the dynamics of liquid vaporization in typical liquid-assisted laser cleaning processes.

The non-intrusive nature and high temporal resolution of optical methods have enabled successful application of several techniques to measurements of various physical quantities in the evaporation process. Optical-reflectance/transmittance methods based on light

* Corresponding author. Present address: Department of Mechanical Engineering, POSTECH, Hoyja 31, Nam-gu, Pohang, 790-784 South Korea. Tel.: +82-54-279-2179; fax: +82-54-279-3199.

E-mail address: dskim87@postech.ac.kr (D. Kim).

[1] Present address: IBM Storage Technology Division, San Jose, CA 95193, USA.

0017-9310/01/$ - see front matter © 2001 Published by Elsevier Science Ltd.
PII: S0017-9310(01)00031-X

Nomenclature

a	characteristic bubble size
c	speed of sound
C_p	heat capacity
d	change in optical path length
$\mathbf{E}_1,\ \mathbf{E}_2$	amplitude of the electric field vectors of reference and probe beams
$\mathbf{E}_{(1)},\ \mathbf{E}_{(2)}$	electric field vectors of reference and probe beams
f	volume fraction of bubbles in a two-phase layer
F	laser fluence
h_{lv}	heat of vaporization
i	imaginary unit, $\sqrt{-1}$
I	electric field intensities, $\lvert\mathbf{E}\rvert^2$ of interference signal
I_{exc}	temporal profile of excimer-laser pulse
$I_1,\ I_2$	electric field intensities, $\lvert\mathbf{E}\rvert^2$ of reference and probe beams
k	thermal conductivity
$\mathbf{k}_1,\ \mathbf{k}_2$	wave vectors of reference beam and probe beam
k_c	constant representing the partial coherence effect
l	length
l_c	distance from the sample surface to the cuvette window
n	complex refractive index
$\bar{n}$	conjugate of n
$n_w,\ n_{vap},\ n_{Cr},\ n_{quartz}$	complex refractive indices of water, water vapor, Cr, and quartz
P	pressure
P_{sat}	saturation pressure
P_v	pressure inside the bubble
P_∞	ambient pressure
$\mathbf{r}$	position vector
R	bubble radius
R_{exc}	reflectivity of excimer-laser on the Cr surface
s	distance
t	time
T	temperature
T_{sat}	saturation temperature
T_v	temperature inside the bubble
V_e	velocity of bubble expansion
x	spatial coordinate normal to the sample surface (positive in the direction into the solid sample)

Greek symbols

α	linear thermal expansion coefficient
δ	effective thickness of the vapor film
δl	change in length by thermal expansion
δT	temperature rise
ε_{eff}	effective dielectric constant
ε_l	dielectric constant of liquid
ε_v	dielectric constant of vapor
$\phi_1,\ \phi_2$	datum phase angles in the reference and probe beam electric fields
γ	absorption coefficient of excimer-laser light in Cr
θ	phase difference
θ_0	constant phase difference between two mutually coherent beams (reference and probe beams), $\phi_2 - \phi_1$
λ	wavelength
ρ	density
$\rho_l,\ \rho_v$	density of water and water vapor
ω	frequency

scattering loss due to bubble growth have been used for the detection of bubble formation, growth, and collapse on a solid surface [5]. An optical-reflectance probe with the aid of an embedded polysilicon thin-film that has highly temperature-dependent and calibrated optical properties has yielded the temperature rise and the degree of superheat during the evaporation process [6]. Finally, an optical beam deflection technique based on the so-called "mirage effect" quantified the pressure transients launched by the pulsed-laser-induced bubble explosion on a Cr surface [7].

The bubble size and the growth rate are the most important physical quantities for understanding the rapid phase-change process, especially the augmented acoustic effect in presence of a liquid layer on a laser-heated solid surface. Nevertheless, the small (submicron) length and short (ns) time scales render the in situ measurement of the size of growing bubbles extremely difficult. When the laser pulse irradiates the solid surface, a number of tiny bubbles nucleate on the surface and then grow. The bubbles may eventually coalesce, in which case the overall number density and shape of the bubble clusters or aggregates are expected to change. Therefore, the presence of multiple bubbles complicates theoretical calculation of the growth rate. Measuring the scattered-light signal by varying the collection angle

is in principle a way to evaluate the bubble size and number distribution. However, appropriate models of the full Maxwell equations should be solved for the interpretation of the experimental data, since the complicated geometry is not amenable to simple analytical solutions. It should also be pointed out that the transient measurement of the low intensity scattered-light distribution poses severe experimental constraints. Consequently, no attempt to measure the size of submicron bubbles growing on a solid surface heated by nanosecond laser pulse has been made so far, although several studies have been performed for larger or stagnant bubbles. For example, Vogel et al. applied high-speed photography and acoustic methods for the investigation of the dynamics of laser-induced cavitation bubbles near a solid surface [9]. Tomita et al. [10] observed cavitation bubbles of millimeter size through high-speed photography at a microsecond time scale. Optical techniques based on Mie scattering were applied to measure the size of spherical bubbles [11,12]. Barber et al. [13] also utilized Mie scattering to measure the radius of micron-size sonoluminescing bubbles. Direct visualization of a cavitation bubble and the emanating pressure field has been conducted using the Mach–Zehnder interferometric technique [14–16]. A high-sensitivity differential interferometer was introduced by Rovati et al. [17] to measure the pulsation of a millimeter-size gas bubble.

This paper utilizes the Michelson interference technique to measure the optical path length change due to vaporization. From the measured optical path change, an effective thickness of the bubble layer is determined under the assumption that this layer can be treated as a single effective two-phase medium. Therefore, the thickness does not directly represent the size of bubbles growing separately on a solid surface. This thickness can be interpreted rather as a quantity proportional to the volume of water vapor. After the bubbles merge, forming a thin-film-like structure, the effective thickness can be regarded as an approximation of the bubble size (bubble layer thickness). In addition to the interference probing, optical-reflectance and scattering measurements are carried by varying the laser fluence. Comparison of the forward-scattering signal with the specular reflectance and interference histories provides information on the overall characteristics of the bubble growth mechanism.

2. Temperature field generated by pulsed-laser heating

The temperature field developed in the excimer-laser-induced vaporization of a liquid in contact with an absorbing solid can be calculated using a one-dimensional heat conduction model. Assuming the laser energy absorption as a volumetric heat generation exponentially decaying from the irradiated solid surface, the energy equation can be written as

$$\rho C_{\mathrm{p}}(T)\frac{\partial T}{\partial t} = \frac{\partial}{\partial x}\left(k(T)\frac{\partial T}{\partial x}\right) + (1-R_{\mathrm{exc}})\gamma I_{\mathrm{exc}}(t)\exp(-\gamma x), \quad (1)$$

where R_{exc} and γ represent the reflectivity at the angle of incidence and the absorption coefficient of the excimer-laser beam ($\lambda = 248$ nm, 24 ns full-width-half-maximum (FWHM)) on a Cr surface, respectively. Calculation of the temperature field has been performed for a thin Cr film (0.3 μm) on a quartz substrate (0.5 mm). The time-dependent variation of the surface temperature at different laser fluences is plotted in Fig. 1. The above model can be used to estimate the temperature field before the liquid temperature reaches the superheat limit at which vaporization commences. Once the bubble nucleation rate is not negligible, Eq. (1) needs to be modified to account for the phase-change process. However, the equation can still be used to obtain an approximate estimate of surface temperature since only a small fraction of heat is transferred to the liquid and the effect of vaporization on surface temperature is small. The validity of the above model was confirmed by the experimental results using photothermal reflectance probe for the in situ measurement of the temperature transients and the degree of superheat [6]. In the study, approximately 90°C of superheat was observed before nucleation in the case of water.

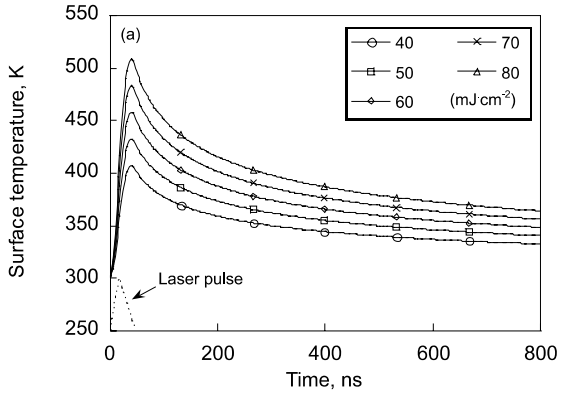

Fig. 1. Calculated temperature increase at the Cr–water interface heated by an excimer-laser pulse with different fluences. The dotted line shows the temporal shape of the laser-pulse intensity in arbitrary units (triangular shape with peak intensity at $t = 17$ ns and width of 48 ns has been assumed).

3. Theory

Michelson interferometry is the best known technique based on the interference effect of two mutually

coherent beams. As mentioned above, the nanosecond-laser-induced bubble growth process can be approximated via invoking the picture of a growing thin vapor film. If the size of individual bubbles in the early stage is much smaller than the wavelength of the probe laser beam, interference technique can be used to monitor the dynamics of vaporization. More precisely speaking, the effective thickness of the bubble layer can be quantified as a function of time. Therefore, the dynamics of vaporization can be examined in a semi-quantitative manner by measuring interference signal. The assumption regarding the effective layer can be justified by the effective medium theory by Maxwell Garnett [18]. According to the theory, the ensemble of small bubble and the liquid can be treated as a single medium with an effective dielectric constant

$$\varepsilon_{\text{eff}} = \varepsilon_{\text{l}}\left[1 - \frac{3f(\varepsilon_{\text{l}} - \varepsilon_{\text{v}})}{2\varepsilon_{\text{l}} + \varepsilon_{\text{v}} + f(\varepsilon_{\text{l}} - \varepsilon_{\text{v}})}\right], \tag{2}$$

where f denotes the volume fraction of the bubbles. In the early stage of bubble nucleation, the effective thickness represents the temporal variation of vapor fraction. As $\sqrt{\varepsilon_{\text{eff}}} = \overline{n}$ by definition, the optical properties of the effective medium can be calculated from ε_{eff}. Two conditions are required for Eq. (2): the bubble size should be small relative to the probe-beam wavelength and the bubbles must be distributed uniformly in the liquid. Consequently, the interference signal has a clear physical interpretation only in the early stage of bubble nucleation or at relatively low laser fluences. The validity of the assumption of effective medium has been verified in the early stage of bubble nucleation by comparing reflectance transients with those by theoretical prediction [5]. As the method by itself does not provide information on the distribution of bubble nuclei, the effective thickness is not directly converted into the bubble size or number density. In this study, scattering and specular reflectance signals are measured as well to obtain the additional information on bubble dynamics. The details of the optical-reflectance and scattering measurements for probing bubble-nucleation process are given in reference [5]. On the other hand, if a vapor film is formed at the solid/liquid interface in the later stage, the effective thickness represents the film thickness.

In the interference technique, the difference between the refractive indices of water vapor and water causes a net change in the optical path length of an interfering beam as the vapor film grows. The schematic diagram of the optical paths is displayed in Fig. 2. The two coherent beams, one serving as reference and the other for detecting the optical path length change, are denoted as 1 and 2, respectively. The resulting electric (magnetic) field is a linear superposition of the corresponding electric (magnetic) field vectors

$$\mathbf{E}_{(\mathbf{1})} = \mathbf{E}_{\mathbf{1}} \exp\left[\mathrm{i}(\mathbf{k}_{\mathbf{1}} \cdot \mathbf{r} - \omega t + \phi_1)\right], \tag{3}$$

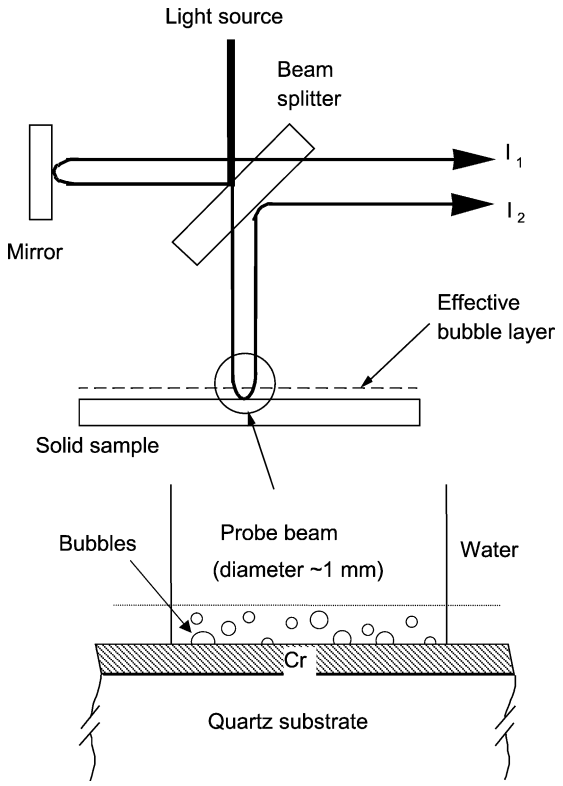

Fig. 2. Beam paths of Michelson interferometry applied to the measurement of vapor-film thickness.

and

$$\mathbf{E}_{(2)} = \mathbf{E}_2 \exp\left[\mathrm{i}(\mathbf{k}_2 \cdot \mathbf{r} - \omega t + \phi_2)\right], \tag{4}$$

yielding the resultant electric field vector

$$\mathbf{E} = \mathbf{E}_{(\mathbf{1})} + \mathbf{E}_{(2)} \ . \tag{5}$$

Therefore, the intensity of the interference signal is proportional to

$$\begin{aligned} I &= |\mathbf{E}|^2 = I_1 + I_2 + 2\mathbf{E}_{\mathbf{1}} \cdot \mathbf{E}_2 \cos\theta \\ &= I_1 + I_2 + 2\sqrt{I_1 I_2}\cos\theta, \end{aligned} \tag{6}$$

where

$$\theta = \mathbf{k}_2 \cdot \mathbf{r}_2 - \mathbf{k}_1 \cdot \mathbf{r}_1 + \phi_2 - \phi_1 = \frac{2\pi d}{\lambda} + \theta_0$$

with d representing the change in the optical path length. The first two terms in Eq. (6) represent the intensities of the probe beams 1 and 2, respectively, while the last term quantifies the interference phase-shift effect. However, the mutual coherence of the two beams is not in general perfect. Hence, in practice the partial coherence of the light yields a smaller interference term than shown in Eq. (6);

$$I = I_1 + I_2 + 2k_{\text{c}}\sqrt{I_1 I_2}\cos\theta, \tag{7}$$

where the partial coherence factor k_c has a value between 0 and 1 ($k_c \approx 0.3$ is obtained in the experiment).

As bubbles grow after the laser pulse, they scatter light, thereby decreasing the specular reflectance of the probe beam. Although the bubble coalescence tends to reduce scattering, the reflectance drop due to the scattering loss cannot be neglected, even when the roughness of the vapor film is very small compared to the probe-beam wavelength. Therefore, the intensity of the reflected beam, I_2, varies as a function of time, while the intensity of the reference beam I_1 is constant. Hence the cosine of the phase angle becomes

$$\cos\theta = \frac{I(t) - (I_1 + I_2(t))}{2k_c\sqrt{I_1 I_2(t)}}, \tag{8}$$

where

$$\theta = \frac{2\pi d}{\lambda} + \theta_0 = \frac{2\pi}{\lambda}\int_C n\,\mathrm{d}s + \theta_0.$$

The beam intensity change, $I_2(t)$ has to be measured separately at the same laser fluence. Therefore, the following relationship between vapor film thickness, δ, and phase angle change, $\theta - \theta_0$, is obtained

$$\theta - \theta_0 = \frac{4\pi\delta}{\lambda} Re\left(n_{\mathrm{vap}} - n_{\mathrm{w}}\right). \tag{9}$$

Due to the nature of the interference technique, only changes in the phase angle, i.e., the thickness of the vapor layer, can be measured, not the direction of change. However, from the physical reasoning that the thickness increases initially and should vary smoothly afterward, the direction can be determined.

In the above model, the reflection of light at the vapor/water interface has been neglected. Since the index of refraction of water ($n_{\mathrm{w}} = 1.34 + 8.16 \times 10^{-10}\mathrm{i}$ at $\lambda = 488$ nm) is different from that of vapor ($n_{\mathrm{vap}} \approx 1$), about 2% of the probe beam is reflected at the interface. The roughness of the vapor film deteriorates the coherence of the internally reflected beams, and tends to suppress multiple beam interference. The maximum uncertainty that may be introduced by multiple beam interference is however estimated by assuming a smooth, planar vapor layer. The characteristic matrix formulation has been applied to calculate the electromagnetic field considering the multiple reflection in the vapor film [19]. Fig. 3 compares the computational results obtained under the two-beam-interference assumption with those considering the multiple-beam-interference effect introduced by the internal reflection in the vapor film ($n_{\mathrm{Cr}} = 2.46 + 4.43\mathrm{i}$ and $n_{\mathrm{quartz}} = 1.46$ at $\lambda = 488$ nm have been used). It is clarified that the two-beam-interference model accounts for the interference between the reference beam and the probe beam whose path length is shifted by the vapor film. In this model, the reflection at the vapor/water interface is not considered. The rigorous

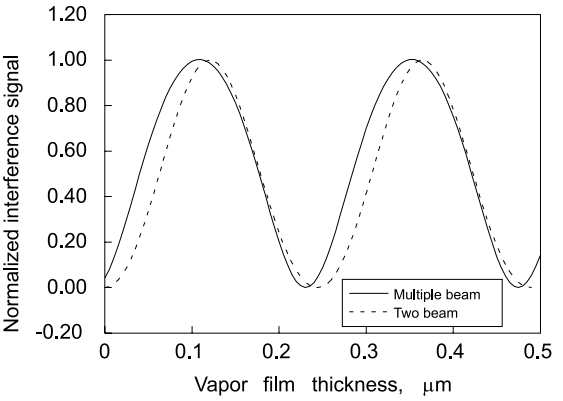

Fig. 3. Calculated interference signal considering the multiple beam-interference effect due to the vapor film and simple two-beam interference (probe beam wavelength = 488 nm).

model including the internal reflection and beam attenuation in the vapor film and the Cr–quartz sample is termed the multiple-beam interference model in this paper. It is noted that the interference effect induced by the Cr–film and quartz substrate appears to be very small due to the strong attenuation of light in the Cr film, i.e., the short optical penetration depth. The calculation has been carried out for the case of two constant interfering beams (I_1 and I_2) assuming that the intensities of the two reflected beams from the sample surface and the mirror are equal. As expected, the two-beam-interference signal exhibits an exact sinusoidal behavior as the thickness of the vapor film increases, while the multiple-beam-interference effect causes a deviation from sinusoidal shape. Since the multiple beam reflection has little effect on the amplitude of the signal and the overall shape can be well approximated as sinusoidal, the two-beam interference model is used throughout this work. However, this approximation causes a maximum measurement uncertainty of about 0.02 μm as shown in the figure.

The phase-change process by short laser pulse is accompanied by rapid temperature rise in the water adjacent to the solid surface. It is also known that a sharp pressure pulse of amplitude reaching about 10 atm is generated at the solid–liquid interface and travels with sonic speed in the water [7]. Since the optical properties of water will be affected by the thermodynamic state, the refractive index change by the temperature and pressure fields should in principle be included in the above model. However, the change is much smaller than the difference between the refractive indices of water and its vapor under the current experimental conditions (for example, $(\partial n/\partial T)_P$ and $(\partial n/\partial P)_T$ values are 0.00015 K^{-1} and 0.00015 MPa^{-1}, respectively, for water near room temperature and atmospheric pressure at $\lambda = 633$ nm [20]). Correspondingly, the effect induced

by the temperature and pressure fields has been neglected in this experiment.

4. Experiments

A schematic diagram of the experimental setup is shown in Fig. 4. A KrF excimer-laser ($\lambda = 248$ nm) with a 24 ns FWHM is used as a heat source. A tunnel-type beam homogenizer of rectangular cross-section makes the excimer-laser beam profile spatially uniform. After passing through the homogenizer, the excimer-laser beam irradiates the solid sample surface at an incidence angle of 30°. The size of the beam spot is about 0.3–0.8 cm^2. The sample consists of a 0.3 μm thick Cr layer on a 0.5 mm thick quartz substrate and the surface roughness is less than 20 nm. A CW Ar ion laser ($\lambda = 488$ nm) is used as an interference probe to detect the bubble growth on the front surface of the sample. The approximate diameter and power of the beam are 1 mm and 50 mW, respectively. Unlike the other mirrors (M1, M2 and M4), a thin Cr film of the same thickness as the sample has been utilized as a mirror for the reference beam (M3) in order to match the reflectance with that on the sample surface. All the mirrors, beam splitters, and sample are mounted on precision stages with adjustable angular positions. The excimer-laser absorption on the Cr-sample surface may induce a high-frequency vibration as it is followed by sharp pressure pulse generation due to rapid thermal expansion and bubble formation. In order to quantify the possible uncertainty due to this vibration, another interferometer has been setup to detect the bulk displacement of the back surface where no phase-change occurs. Therefore, the two interference signals (front probe for detecting optical path length change due to the vapor film growth and the other for detecting the mechanical vibration of the sample) are monitored simultaneously. A He–Ne laser beam ($\lambda = 633$ nm; 10 mW) is used as interference probe for the vibration detection. The signals are detected by fast photodetectors (rise time < 1 ns) and the digitized signal is captured by an 8-bit digital oscilloscope (HP 54510A) connected to a PC.

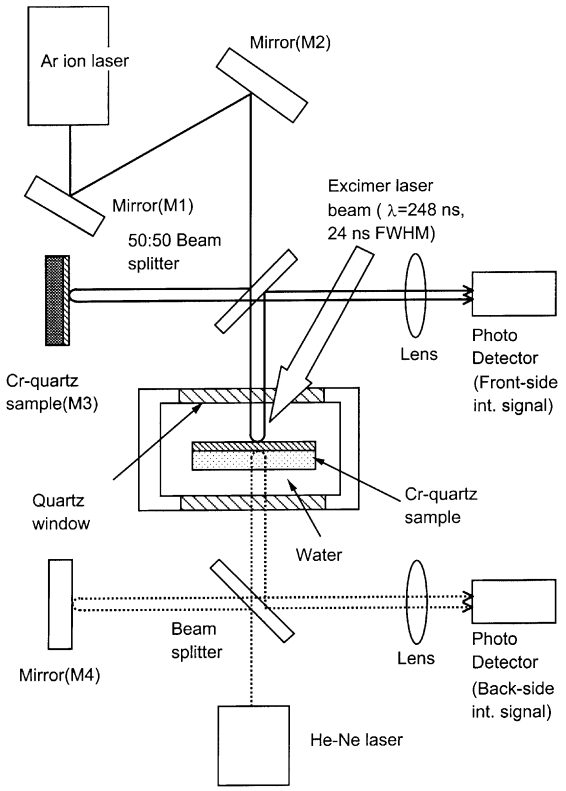

Fig. 4. Schematic diagram of experimental setup using two Michelson interferometers (front-surface probe and back-surface probe) for measuring the optical path length change due to bubble formation on a Cr surface and for monitoring the solid sample vibration, respectively.

In Eq. (8), I_2 is not constant, but rather a time-dependent quantity, because of scattering. Therefore, after measuring the interference signal, $I_2(t)$ is measured with the reference beam I_1 blocked by replacing M3 with a non-reflecting beam stop. The signal measured in this configuration represents a pure normal–incidence–reflectance change without any interference effect.

In order to verify the correct setup of the interferometers, a simple displacement measurement has been performed. The solid sample is mounted on a micrometer stage and no water is filled in the cuvette. Instead of the excimer-laser heating, the sample stage is displaced using the micrometer and the corresponding interference signals are recorded. Fig. 5 compares the two interference signals (one from the front surface and the other

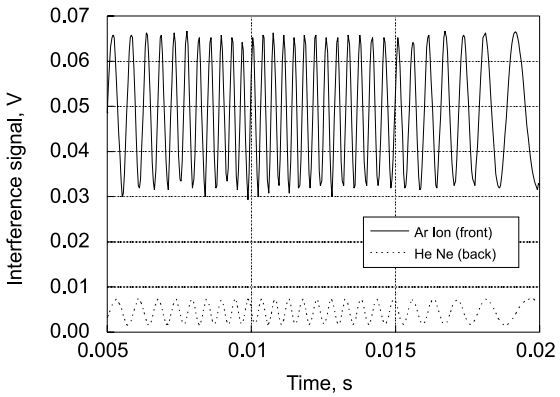

Fig. 5. Interference fringes obtained with two different probe laser beams for the measurement of the bulk displacement of the solid sample.

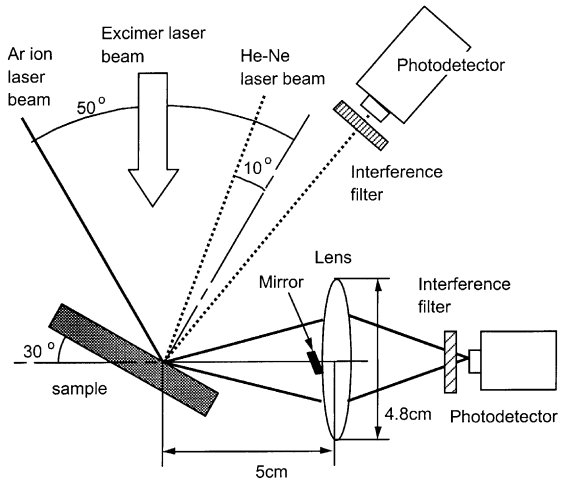

Fig. 6. Experimental setup for the measurement of the scattering signal due to the bubble generation on a Cr surface heated by an excimer-laser beam.

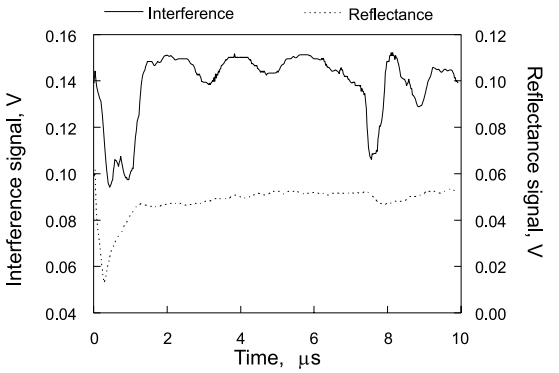

Fig. 7. An example of long-term transient interference and reflectance signals induced by the bubble growth on a Cr surface. Laser fluence is about 60 mJ/cm^2.

from the back surface). The number of fringes generated by Ar ion laser is 31 and that by He–Ne laser is 24. The ratio of the number of fringes by Ar ion laser to that by He–Ne laser is 1.29. This value is very close to the inverse of the ratio of the respective wavelengths (633/488 = 1.30). The number of fringes also exactly corresponds to the displacement of the micrometer stage (15 μm). This experiment confirms the correct setup of the interferometer.

Since the quantity obtained by the interference signal is the 'effective' vapor film thickness, rather than the physical thickness of the bubble layer, additional information about the bubble growth characteristics is required for the interpretation of the interference signal. For this purpose, simultaneous measurements of light scattering and specular reflectance are performed in addition to the previously mentioned normal–incidence–reflectance (I_2) measurement. The experimental arrangement for the forward-scattering measurement is depicted in Fig. 6. For the scattering probe, the Ar ion laser ($\lambda = 488$ nm) is again utilized. The specularly reflected beam is blocked by a small mirror, thus allowing only the forward-scattering signal. The collection full polar angle of the scattered light is set to 51° (solid angle = 0.72 sr). The He–Ne laser beam ($\lambda = 633$ nm) shown in Fig. 6 monitors the specular reflectance to detect the bubble formation and growth dynamics simultaneously with the scattering probe.

5. Results and discussion

A typical interference signal that reflects the bubble kinetics is shown in Fig. 7. The figure exhibits simultaneously measured interference and reflectance signals. The amplitudes of the early signals representing the initial vaporization phenomena are comparable in magnitude for both the interference and reflectance probes. On the other hand, the second fall at about 8 μs, which is induced by the long-term memory effect [5], is much more distinct in the case of interference probe. It has been revealed that acoustic cavitation by a reflected pressure wave can result in substantial bubble formation even after a long period of time [5]. In this study, the acoustic pulse initially emitted from the Cr surface returns to the surface after being reflected by the quartz window of the cuvette, which induces acoustic cavitation at a temperature far below the saturation point. The time that the second peak of the interference signal (~8 μs) appears corresponds to the arrival time of the acoustic pulse, i.e., $2l_c/c$. Fig. 7 manifests that a thin layer of bubbles persists at the interface for a significant amount of time after the initial bubble nucleation.

The measured effective film thickness of the bubble layer and the corresponding reflectance signal are displayed in Figs. 8(a) and (b). The thickness of the vapor film starts to increase rapidly after the laser-pulse absorption and has a maximum value at a few hundred nanoseconds after the laser pulse. The reflectance signal decreases until 150 ns, and then gradually recovers. In the period from 150 to 400 ns, the effective film thickness increases, while the amount of reflectance drop decreases, indicating that the light scattering loss is recovered in spite of the increasing size of the vapor film. Therefore, it is expected that the bubbles which were growing separately in the initial stage have already started to coalesce. It is also noted that the deduced effective thickness becomes a close approximation of the vapor film thickness in this regime. Comparison of the measured effective thickness with the results in Fig. 1(b) indicates that the film can grow further beyond the superheated region in water owing to the inertia of the

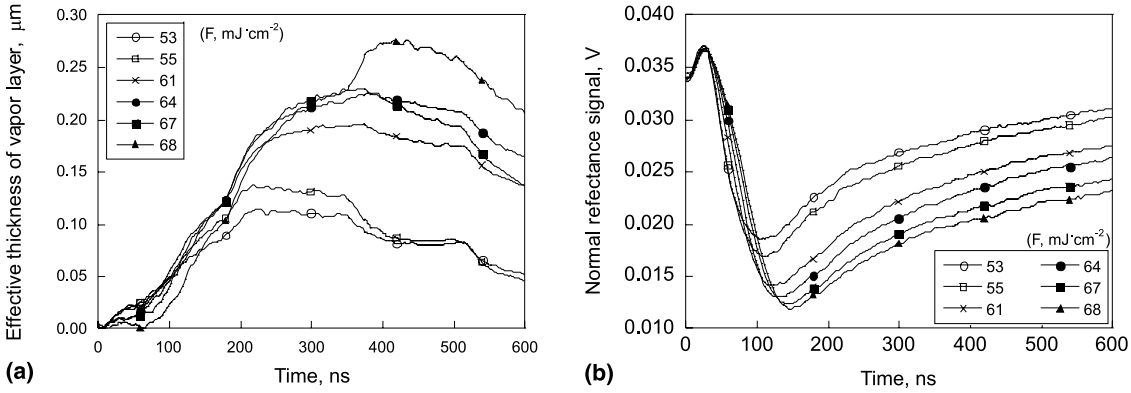

Fig. 8. (a) Effective thickness variation of the bubble layer (solid lines) and the back surface movement (dotted lines) measured by the optical path length change at different laser fluences; (b) the corresponding normal–incidence–reflectance signal on the vapor-covered surface. The laser beam is unpolarized.

expanding vapor film. However, it starts to decay due to the lack of sufficient heat and momentum supply after the film grows to maximum thickness.

The dotted lines in Fig. 8(a) represent the change in optical path length due to mechanical vibration measured by the back-side interferometer which detects the movement of the back surface of the sample where no phase-change occurs. Since the direction of the movement, however, cannot be determined by the interference signal, no correction for this error is possible. Therefore, the maximum magnitude of these signals at each laser fluence should be regarded as indicative of the uncertainty in the vapor layer thickness measurement. This uncertainty is thus shown to be about 8% around the maximum vapor film thickness (200–500 ns). It is also estimated that the error induced by this mechanical vibration is the biggest contributor to the overall uncertainty. Two main sources of high-frequency mechanical vibration are the thermoelastic expansion of the solid sample due to temperature rise and the pressure pulse generated by phase-change. The whole experimental setup was built on an optical table equipped with pneumatic isolators to suppress environmental vibration, whose effect has been additionally examined by observing the interference signal without excimer-laser heating. The interference signal shows no change in the time range of the current experiment, since the period of typical environmental vibration is in millisecond range, which is much larger than the time scale of this experiment. Therefore, the possibility of inadvertent background mechanical vibration is ruled out.

In order to clarify the main source of this high-frequency vibration and estimate the thermal deformation effect on the sample surface excluding the phase-change effect, an interference signal was taken from a dry (i.e., not immersed in water) sample. The results show that over the entire laser-fluence range from 50 to 70 mJ/cm^2, the change in optical path length is smaller by more than an order of magnitude than that with water. This confirms experimentally that the main source of the high-frequency vibration is indeed the pressure pulse generation in the liquid, with essentially negligible contribution by thermal expansion. The order of magnitude of the thermal expansion of the Cr surface can be estimated in terms of the linear expansion coefficient ($\alpha = 6 \times 10^{-6}$ K^{-1}) and the temperature rise δT as

$$\frac{\delta l}{l} = \alpha \delta T. \tag{10}$$

For laser fluence $F = 70$ mJ/cm^2, $\delta l/l$ is calculated to be about 0.001 by substituting the maximum temperature rise (about 180 K as shown in Fig. 1) for δT. Assuming that the expansion occurs uniformly within the thermal penetration depth range (~1 μm), the magnitude of the surface displacement δl is estimated to be of the order of 1 nm. Thermoelastic expansion occurs over a period comparable to the time scale of the heat source (laser pulse width ~48 ns). However, the back side signal in Fig. 8(a) increases monotonically over the entire measurement range up to 600 ns. This provides further evidence that the main source of the interference signal from the back surface is phase-change, followed by strong pressure pulse emission.

The results of forward-scattering measurements are plotted in Fig. 9 for various laser fluences. The figure contains the scattering and reflectance data at laser fluences above 65 mJ/cm^2 since the amplitude of the scattering signal below this fluence is so weak that it becomes comparable to the noise level. The dotted lines in the figure denote the corresponding reflectance drop. Amplitudes of both the reflectance drop and the forward-scattering signal increase with laser fluence as expected. The scattering signal has a maximum value at

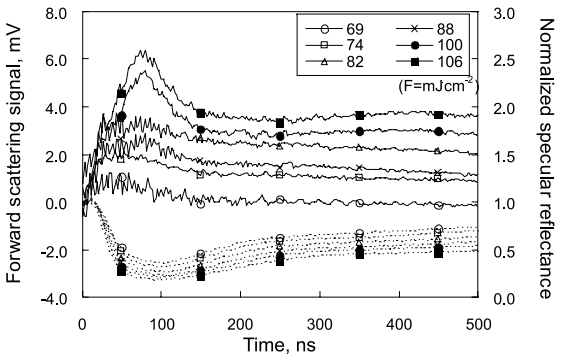

Fig. 9. Transient forward-scattering signal (solid lines; collection solid angle = 0.72 sr) and the corresponding specular reflectance signal normalized by the initial intensity (dotted lines; incident angle = 10°) induced by the bubble growth on a Cr surface for various laser fluences. A CW Ar ion laser beam ($\lambda = 488$ nm, unpolarized) and a CW He–Ne laser beam ($\lambda = 633$ nm, unpolarized) are utilized for the scattering and reflectance measurements, respectively.

about 100 ns, which roughly corresponds to the minimum of the reflectance signal. This result confirms that the extinction in the reflectance signal is largely due to pure scattering by the nucleating bubbles. It is pointed out that the effective thickness obtained from the interference signal does not have a simple physical interpretation based on Eq. (2) if Mie scattering dominates, i.e., $a \gg \lambda/2\pi Re(n_w)$. Accordingly, an alternative interpretation of the interference signal is possible in the regime, where relatively large bubbles exist separately.

A notable change in the shape of the scattering signals is observed in Fig. 9 as the laser fluence increases. While the forward-scattering signal at low laser fluences decreases monotonically after the peak, at high fluences (above 95 mJ/cm^2, approximately) it has a second, discernible though smaller elevation at about 400 ns. The increase in overall scattering cross-section implies an increase in bubble size or a change in bubble geometry (number, shape, and so on). Therefore, the enhancement of the forward-scattering signal could be ascribed to a change in bubble number density (i.e., breaking of the vapor film into small bubbles due to instability) or in the shape of the bubbles (i.e., change in surface roughness of the film). It is noted that the reflectance signal still recovers, but at a substantially slower rate. If independent scattering by a cloud consisting of many bubbles is assumed, extinction cross-sections of the single bubbles can be added to give the corresponding cross-sections for the entire cloud [21]. However, the linear relationship cannot be employed in the present work, as the validity of the assumption of independent scattering is unknown except for the very early stage.

On the basis of the above-mentioned observation through the interference and scattering measurements, four distinct regimes of bubble growth are suggested as follows:

- *Regime I (~150 ns)*. Both the size and the number density of the bubbles increase, resulting in increases of both the scattering loss and the interference signal (effective thickness of the bubble layer).
- *Regime II (150–400 ns)*. The size (volume fraction) of bubbles increases, but the number density decreases, manifested by recovery of the scattering loss and increase in the effective thickness. Bubbles may coalesce in this regime and the layer of bubbles can be well approximated as a thin vapor film.
- *Regime III (around 450 ns, at laser fluences above 95 mJ/cm^2)*. When the film thickness exceeds a certain limit, instability causes a change in the structure of the vapor film. At higher laser fluences, a second elevation of the scattering signal is observed, indicating a possible change of the vapor layer morphology. The effective thickness attains a maximum value around this point, while the reflectance drop recovers.
- *Regime IV (500 ns ~)*. The size and number density of the bubbles are reduced, resulting in decrease of both the scattering loss and the effective thickness of the bubble layer.

The early stage of bubble growth is largely dominated by an inertia-controlled process. In this case, the growth rate of a spherical bubble on a solid surface (contact angle 0°) adjacent to uniformly superheated liquid is [22,23]

$$R = \sqrt{\frac{\pi}{7}\frac{P_v - P_\infty}{\rho_l}}t. \tag{11}$$

For a rough estimate (of the order of magnitude) of the bubble growth rate, the temperature field is assumed to be uniform around the bubble and the pressure difference term is approximated using the Clausius–Clapeyron equation

$$P_v - P_\infty = \frac{\rho_v h_{lv}[T_v - T_{sat}(P_\infty)]}{T_{sat}(P_\infty)}. \tag{12}$$

Substituting T_v with the maximum Cr-surface temperature calculated by Eq. (1) yields an upper limit of the bubble growth rate encountered in the experiment. The estimated values are 10–14 m/s in the laser fluence range from 50 to 70 mJ/cm^2. It is cautioned that Eq. (11) assumes constant superheat of liquid as well as a single spherical bubble on a solid surface. It is therefore very likely that these estimates actually overpredict the bubble growth rate even in the very early stage prior to merging. On the other hand, the growth rate of the effective vapor film in the initial stage (regime I) ranges from 0.5 to 1 m/s as given by Fig. 8(a). Since, as

mentioned previously, the effective layer thickness does not directly represent bubble size, these values are considered as lower limits of the bubble growth rate. Hence, it is demonstrated that the bubble growth rate in the early stage (inertia controlled regime) is of the order of 1 m/s. On the other hand, Fig. 8(a) shows that the bubble collapse rate is smaller than the initial growth rate. Accordingly, it is concluded that the acoustic enhancement in the vaporization process is caused by the initial bubble expansion, not by the cavitation pressure following rapid bubble collapse. The order of magnitude of the acoustic augmentation by vaporization is estimated as $P \sim \rho c V_e \sim O$ (1 MPa). These observations are consistent with the finding by the pressure measurement [7].

It has been shown in the present work that the optical interference measurement is more sensitive than typical reflectance probes and thus effective for analyzing rapid-vaporization phenomena. However, it is again noted that the measurement is complete only when the physical interpretation of the effective thickness is available. In the present study, light-scattering intensity has been measured, resulting in the suggested mechanisms of bubble nucleation. However, for the bubble sizing to be quantitative, rigorous scattering measurements must be performed for a wide range of parameters, such as scattering intensity, scattering angle, probe-beam wavelength, and polarization. As the size parameter of the bubbles $2\pi Re(n_w)a/\lambda$ changes as a function of time, multiple scattering parameters are needed to ensure the sensitivity of measurement in the entire range.

6. Conclusions

The Michelson interference technique has been applied to measure, for the first time, the effective thickness of a rapidly growing bubble layer in water on a pulsed-laser-heated solid Cr film on a quartz substrate. The maximum size and growth rate have been estimated to be of the order of 0.1 μm and 1 m/s, respectively, for laser fluences ranging from 50 to 70 mJ/cm^2. The interferometry is combined with forward-scattering and specular reflectance measurements to further elucidate the bubble nucleation and growth mechanism. The results show that separate, isolated bubbles nucleate and grow in the early stage, and coalesce when their size exceeds a certain limit. The vapor film decays monotonically after reaching a maximum thickness at moderate laser fluences. However, a second elevation in the forward-scattering signal is observed above this laser fluence suggesting that a change in the structure of the vapor film is induced by instability of the vapor/liquid interface. These results indicate that the initial bubble expansion is responsible for the augmented photoacoustic effect in the liquid vaporization process.

Acknowledgements

Support for this work by DOE under Grant DE-FG03-95ER14562 is gratefully acknowledged. The authors thank Xiang Zhang for the fabrication of samples. The work was conducted at the Laser Thermal Laboratory of the Department of Mechanical Engineering, University of California at Berkeley.

References

[1] V.P. Skripov, Metastable Liquids, Wiley, New York, 1974.
[2] S.V. Stralen, R. Cole, Boiling Phenomena, vol. 1, 2, Hemisphere, Washington, DC, 1979.
[3] V.P. Carey, Liquid–Vapor Phase-Change Phenomena, Hemisphere, Washington, 1992.
[4] A.C. Tam, W.P. Leung, W. Zapka, W. Ziemlich, Laser-cleaning techniques for removal of surface particulates, J. Appl. Phys. 71 (1992) 3515–3523.
[5] O. Yavas, P. Leiderer, H.K. Park, C.P. Grigoropoulos, C.C. Poon, W.P. Leung, N. Do, A.C. Tam, Optical reflectance and scattering studies of nucleation and growth of bubbles at a liquid–solid interface induced by pulsed laser heating, Phys. Rev. Lett. 70 (1993) 1830–1833.
[6] H.K. Park, X. Zhang, C.P. Grigoropoulos, C.C. Poon, A.C. Tam, Transient temperature development during the vaporization of liquids on a pulsed-laser heated solid surface, ASME Trans. J. Heat Transfer 118 (1995) 702–708.
[7] H.K. Park, D. Kim, C.P. Grigoropoulos, Pressure generation and measurement in the rapid vaporization of water on a pulsed-laser-heated surface, J. Appl. Phys. 80 (1996) 4072–4081.
[8] M. Geiger, W. Becker, T. Rebhan, J. Hutfless, N. Lutz, Increase of efficiency for the XeCl excimer laser ablation of ceramics, Appl. Surf. Sci. 96–98 (1996) 309–315.
[9] A. Vogel, W. Lauterborn, R. Timm, Optical and acoustic investigations of the dynamics of laser-produced cavitation bubbles near a solid surface, J. Fluid Mech. 206 (1989) 299–338.
[10] Y. Tomita, A. Shima, High-speed photographic observations of laser-induced cavitation bubbles in water, Acustica 71 (1990) 161–171.
[11] G.M. Hansen, Mie scattering as a technique for the sizing of air bubbles, Appl. Opt. 24 (1985) 3214–3220.
[12] R.G. Holt, L.A. Crum, Mie scattering used to determine spherical bubble oscillations, Appl. Opt. 29 (1990) 4182–4191.
[13] B.P. Barber, S.J. Putterman, Light scattering measurements of the repetitive supersonic implosion of a sonoluminescing bubble, Phys. Rev. Lett. 69 (1992) 3839–3842.
[14] B. Ward, D.C. Emmony, Interferometric studies of the pressures developed in a liquid during infrared-induced cavitation-bubble oscillation, Infrared Phys. 32 (1991) 489–515.
[15] B. Ward, D.C. Emmony, Direct observation of the pressure developed in a liquid during cavitation bubble collapse, Appl. Phys. Lett. 59 (1991) 2228–2230.
[16] A.P. Alloncle, D. Dufresne, M. Autric, Visualization of laser-induced vapor bubbles and pressure waves, in:

J.R. Blake (Ed.), in: Bubble Dynamics and Interface Phenomena, Kluwer Academic Publishers, Netherlands, 1994, pp. 365–371.

[17] L. Rovati, P. Lago, M. Corti, C. Gomarasca, Optical interferometer for gas bubble vibration measurements with angstrom sensitivity, Rev. Scientific Instr. 64 (1993) 1463–1467.

[18] J.C. Maxwell Garnett, Colours in metal glasses and in metallic films, Philos. Trans. Roy. Soc. 203 (Ser. A) (1904) 385–420.

[19] M. Born, E. Wolf, Principles of Optics, Pergamon Press, Oxford, 1980, Chapter 7.

[20] P. Schiebener, J. Straub, J.M.H. Levelt Sengers, J.S. Gallagher, Refractive index of water and steam as function of wavelength, temperature, and density, J. Phys. Chem. Ref. Data 19 (1990) 677–717.

[21] H.C. van de Hulst, Light Scattering by Small Particles, Dover, New York, 1957.

[22] C.P. Witze, V.E. Schrock, P.L. Chambre, Flow about a growing sphere in contact with a plane surface, Int. J. Heat Mass Transfer 11 (1968) 1637–1652.

[23] B.B. Mikic, W.M. Rohsenow, P. Griffith, On bubble growth rates, Int. J. Heat Mass Transfer 13 (1970) 657–666.